

Research Article

Hydrodynamic Characterization of the *Polyodon spathula* Rostrum Using CFD

Jeffrey B. Allen and Guillermo Riveros

Information Technology Laboratory, US Army Engineer Research and Development Center, ATTN: CEERD-IE-C,
3909 Halls Ferry Road, Vicksburg, MS 39180, USA

Correspondence should be addressed to Jeffrey B. Allen; jeffrey.b.allen@usace.army.mil

Received 9 July 2013; Accepted 14 September 2013

Academic Editor: Tin-Tai Chow

Copyright © 2013 J. B. Allen and G. Riveros. This is an open access article distributed under the Creative Commons Attribution License, which permits unrestricted use, distribution, and reproduction in any medium, provided the original work is properly cited.

Among the various functions of the paddlefish rostrum, it is also believed to serve as a stabilizer to counteract the downward force that would otherwise occur during the process of filter feeding. From its unique shape, it is hypothesized that the paddlefish rostrum serves to generate a substantial amount of lift that naturally occurs as the rostrum is elevated at the same time the fish opens its mouth. The present, numerical study is an attempt to quantify the amount of lift (and drag) that is generated by the rostrum of a juvenile paddlefish. Additionally, this data is compared with other hydrofoils. The results suggest that the paddlefish rostrum does indeed produce substantial lift at certain angles of attack. In fact, the results indicate that the amount of lift is comparable to that produced by a symmetric foil (NACA 0012).

1. Introduction

The paddlefish, *Polyodon spathula*, are among the most primitive of bony-finned fishes (Osteichthyes, Actinopterygii) and together with sturgeon comprise an order of secondary cartilaginous fishes, the Acipenseriformes [1]. While originally ranging throughout much of the Mississippi River drainage and eastward of the Appalachian Mountain range, unfortunately, due to overexploitation, reservoir construction, and other factors, they are currently imperiled in many of their original habitats [2]. Weighing up to 200 lbs, with lengths approaching 84 in, the fish are one of the largest riverine species in the world [3]. Analogous to baleen whales, their bulk is primarily attributable to their filter feeding of plankton material.

With respect to their preferred habitat, paddlefish typically occupy deep slow-moving currents within large river systems. They tend to seek out natural riverine corridors, often created by deep eddies behind gravel bars. In modified rivers, paddlefish will often use deep eddies and backwaters created by wing dams and other man-made structures [4].

The physiologically distinctive paddle or rostrum accounts for approximately one-fourth to one-third of the

length of the body (see Figure 1). In juvenile paddlefish, the rostrum may account for even greater proportions [5]. Unlike other marine animals with similar physiologies (i.e., long noses or jaws), the paddlefish rostrum is unique in that it is an elongation of its cranium [1].

One important function of the rostrum has been correlated with the fish's ability to find food. In various feeding experiments, it has been observed that juvenile paddlefish readily capture plankton (*Daphnia*) without the benefit of using their visual, chemical, or hydrodynamic senses [6]. This finding suggests the existence of an alternate sensory mechanism. Similar to the platypus bill, the paddlefish rostrum is known to be covered by an extensive array of electroreceptors [7]. The rostrum thus serves as a type of antenna, a sensory device with sufficient sensitivity to detect the electric fields of their planktonic prey [8, 9].

Another important function of the rostrum, serving as the primary objective of the present study, is that it is believed to serve as a stabilizer to prevent a nose diving that would otherwise occur as a result of the drag created by water entering the gaping mouth during filter feeding [10]. According to the observed actions that occur during filter feeding, the expansive mouth cavity (see Figure 1) takes in



FIGURE 1: Photograph of a feeding paddlefish. Photograph reproduced with permission from Pettigrew and Wilkens [1].

such massive quantities of water that the combined weight and pressure drag associated with this particular feeding action would render most fish in complete disequilibrium (causing a nose dive). Fortunately, the paddlefish rostrum acts to counteract this downward force with an opposing lift force, which naturally occurs as the rostrum is elevated (creating an angle of attack relative to the free-stream current) at the same time the fish opens its mouth.

The present, numerical study is an attempt to quantify the amount of lift and drag force that act on the rostrum during these observed feeding actions. To outline the course of action for the remainder of this work, first, the geometry of juvenile paddlefish rostrum is modeled from a recently deceased specimen of approximately three years of age; second, an appropriate turbulence model suitable for conditions involving boundary layer flow separation (a condition likely to exist along the surface of the rostrum) is selected and validated with experimental data; third, the validated model is applied to the paddlefish rostrum using three separate angles of attack; and finally the results are compared with computed and existing hydrofoil data, all at equivalent Reynolds numbers and characteristic length scales. It is hoped that this study will provide some additional insights into the unique capabilities of this endangered species and prompt further interest in safeguarding its future.

2. Numerical Modeling of the Rostrum Geometry

The paddlefish rostrum was modeled from a selection of 3D point cloud data corresponding to a juvenile specimen of approximately 3 years of age and at an initial resolution of approximately $1\text{E-}3$ m. As indicated in Figure 2, a reference length (d) of 0.26 m was assigned extending from the tip of the rostrum ($x = 0$ m) to its base ($x = 0.26$ m). The maximum thickness of the rostrum was approximately 0.045 m and was located, as shown in Figure 1, at $x = 0.26$ m. The initial geometry was modeled with the assistance of various computer aided drafting tools, including 3DS MAX [11].

As shown in Figure 3, the overall solution domain extends approximately 0.6 m in each direction and was thus sized in order to avoid unrealistic boundary effects. The geometry was meshed using GAMBIT [12] and a hybrid combination of nonconformal, unstructured, tetrahedral, and hexahedral elements was used. A size function application was utilized that allowed for localized mesh refinement at the surface of the rostrum. The graded mesh, governed by a first cell

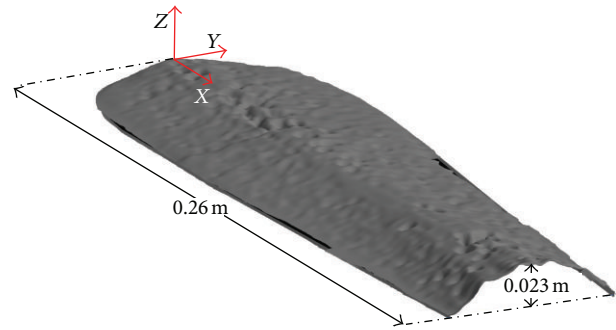


FIGURE 2: Upper surface geometry of the paddlefish rostrum, also showing location of reference coordinate system.

height of approximately 0.001 m, resulted in a value for the nondimensional viscous wall unit (y^+) of approximately 30. This result resides at the lower limit for log law applications $30 < y^+ < 500$ [13] and is within the desired accuracy limits of the turbulence validation model (see Section 3). Mesh coarsening of the surrounding cells was based on a 10% maximum successive increase and culminated in a maximum allowable edge length of approximately 0.01 m.

3. Turbulence Model Selection/Validation

One of the more challenging problems associated with turbulence modeling is the accurate prediction of boundary layer flow separation from solid surfaces. While Large Eddy Simulation (LES) has in recent years assumed the predominant role for these types of simulations, a growing number of Reynolds Averaged Navier Stokes (RANS) based turbulence closure models have also shown significant promise. Compared to LES, RANS based models, although inherently less accurate, are attractive due to their relative simplicity and low computational costs. Typical LES simulations intrinsically require very high spatial and temporal resolution in order to adequately resolve the large scale turbulent eddies. Additionally, the ensemble averaging, which is required for the computation of various mean field quantities, requires relatively long integration times. RANS simulations, in contrast, typically require only a few shedding periods in order to converge to time averaged results.

In a recent study [14], three RANS, two-equation, linear eddy viscosity turbulence models were compared with the experimental benchmark results pertaining to a turbulent flow over a square cylinder [15, 16]. Figure 4 shows the relevant geometry and mesh. The motivation for the study was to evaluate the effectiveness of these RANS based models when applied to applications involving boundary layer flow separation. In particular, the study compared results using the standard $k-\epsilon$ turbulence model [17], the Renormalization Group (RNG) $k-\epsilon$ model [18], and the shear-stress transport $k-\omega$ model (SSTKW) [19]. While the details are not presented here, the results pertaining to the time averaged, streamwise velocity are shown in Figure 5.

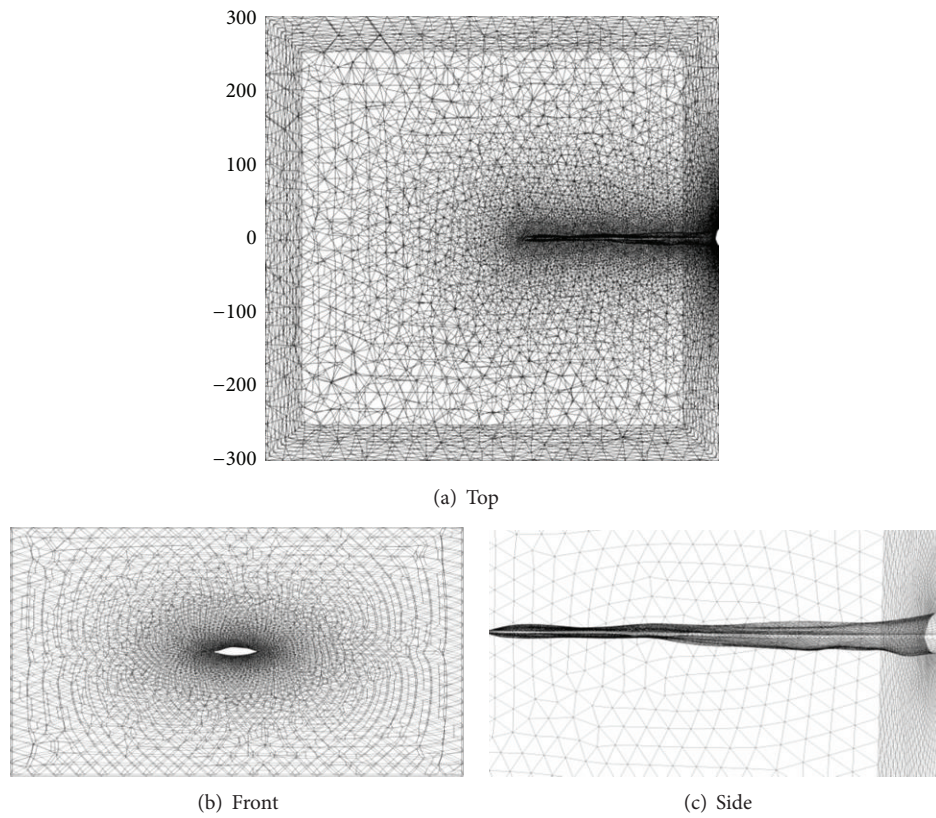


FIGURE 3: Paddlefish mesh showing domain extents and top front and side views.

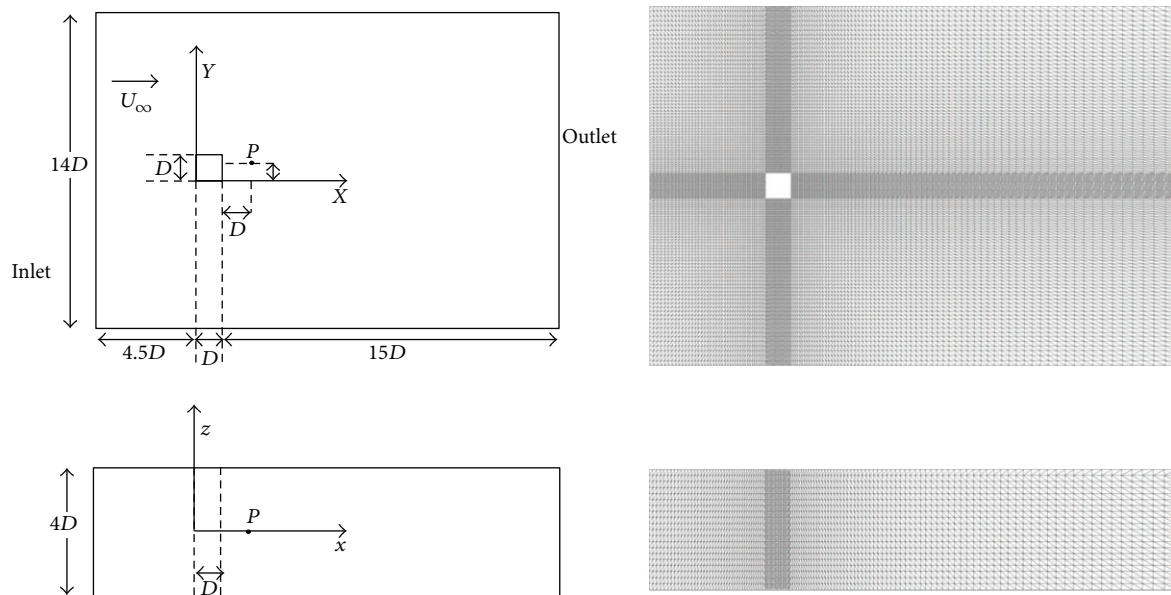


FIGURE 4: The geometry and mesh of the square cylinder validation case (Lyn et al. [15, 16]). Based on the rectangular side length D (where $D = 0.04$ m), a domain of size $21.5D \times 14D \times 4D$ was formed. Two different, nonuniform, hexagonal mesh densities were created; the first was composed of $130 \times 120 \times 20$ cells ($y^+ = 100$), and the second was composed of $180 \times 180 \times 40$ cells ($y^+ = 30$).

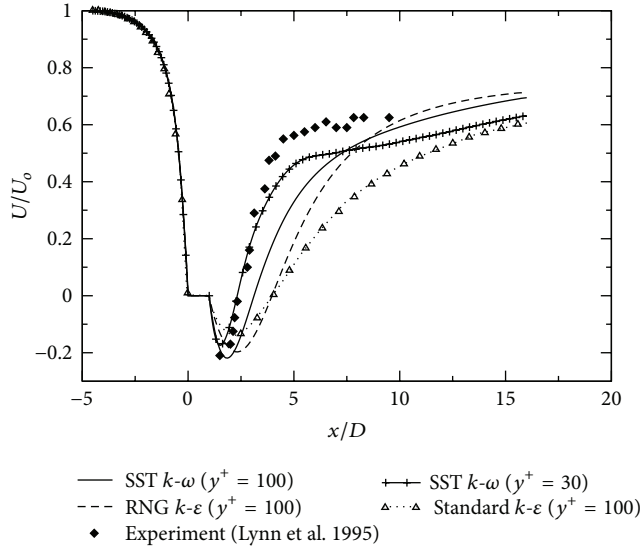


FIGURE 5: The time averaged, streamwise velocity component along the domain centerline ($-4.5 \leq x/D \leq 16$, $y/D = 0.5$, $z/D = 0$) comparing the SKE, RNGKE, and the SSTKW turbulence closure models with the experiments performed by Lyn et al. [15, 16]. The SSTKW model with near wall resolution, $y^+ = 30$ (where y^+ is a nondimensional, viscous wall unit [13]), shows the best agreement with experiment. It predicts a minimal velocity of approximately -0.2 at $x/D = 1.7$ and a return to the free-stream velocity that is significantly faster than any other model.

As indicated, there is excellent agreement between the experimental results and all of the turbulence models forward of $x/D = 0$ (corresponding to the front leading edge of the square cylinder). Aft of the cylinder ($x/D = 1$), however, boundary layer flow separation begins to take effect, and there are noticeable differences among the models. As shown, of all the cases, the SSTKW model with near wall resolution $y^+ = 30$ (where y^+ is a nondimensional, viscous wall unit [13]), shows the best agreement with experiment. It predicts a minimal velocity of approximately -0.2 at $x/D = 1.7$ and a return to the free-stream velocity that is significantly faster than any other model.

These promising initial results prompted additional comparison studies involving the SSTKW model. These included the evaluation of the Strouhal number (St) and the lift and drag coefficients, C_l and C_d , respectively. Table 1 shows comparisons of these values with the experimental work of Lyn et al. [15, 16] as well as Direct Numerical Simulation (DNS) and LES simulations conducted by Versteppen and Veldman [20], Nozawa and Tamura [21], respectively. As shown, the Strouhal number predicted by the use of the SSTW model is identical to the DNS results. The C_l and C_d values were also shown to be respectable, and in the former case, within the range predicted by the LES and DNS numerical results. These results confirmed the appropriate use of the SSTKW model for this work.

4. Simulation Setup for the Paddlefish Rostrum

An inlet velocity of 0.5 m/s was assigned to the inlet face as well as all top/bottom faces of Figure 3 in accordance with

TABLE 1: Comparisons of average C_l , C_d and St.

Reference	$\langle C_l \rangle$	$\langle C_d \rangle$	St
Versteppen and Veldman (DNS) [20]	0.005	2.09	0.133
Nozawa and Tamura (LES) [21]	0.0093	2.62	0.131
Experiment: Lyn et al. [15, 16]	—	2.1	0.132
Present work (SST $k-\omega$)	0.0071	1.75	0.133

typical stream velocities to which North American sturgeon and paddlefish are accustomed [22]. Using a reference length ($d = 0.26$ m) and a kinematic viscosity (based on a temperature of 20°C) of $1.0E-6$ m²/s resulted in an average Reynolds number of $1.3E5$ and was thus considered well within the turbulence flow regime. The outlet boundary condition was implemented using a zero velocity gradient and a constant pressure condition of 0 Pa (gauge). The rostrum itself was modeled with a zero-slip boundary condition.

As a result of the aforementioned turbulence model results of Section 3, the SSTKW turbulence closure method (with $y^+ \leq 30$) was used. The inlet turbulence values associated with the turbulent kinetic energy (k), the turbulent dissipation rate (ϵ), and the specific dissipation rate (ω) were computed from the usual, approximate relations [13]:

$$\begin{aligned}
 k &= 1.5(U_i T_i)^2, \\
 \epsilon &= \frac{C_\mu^{0.75} k^{1.5}}{L}, \\
 \omega &= \frac{k^{0.5}}{C_\mu^{0.25} L},
 \end{aligned} \tag{1}$$

where U_i is the inlet velocity, T_i is the turbulence intensity ($T_i = 0.16(\text{Re})^{1/8}$), k is the turbulent kinetic energy, C_μ is an empirically based numerical constant ($C_\mu = 0.0845$), and the turbulence length scale (L) was taken as $0.07d$ (the factor 0.07 is based on the maximum mixing length in a turbulent pipe flow).

The pressure-based, finite-volume code, Fluent Version 13.0 [23], was utilized to solve the three-dimensional conservation equations pertaining to mass, momentum, and turbulence transport. Interpolation to cell faces for the convection terms was performed using the second-order upwind discretization scheme, while second-order central differences were utilized for the viscous terms. Pressure-velocity coupling was based on the Pressure Implicit with Splitting of Operators (PISO) method [24]. Prior to running the SSTKW model, the simulations were initialized using the converged, steady-state results of a standard k -epsilon turbulence model. The simulations were run on an in-house Cray XT4 supercomputer using 16 core processors, with average run times of approximately 3 hrs.

The steady-state solutions were considered converged when residuals for each of the governing equations (based on the L2 norm) were reduced by a minimum of five orders of magnitude, and time-history plots of the lift and drag coefficients showed minimal variation.

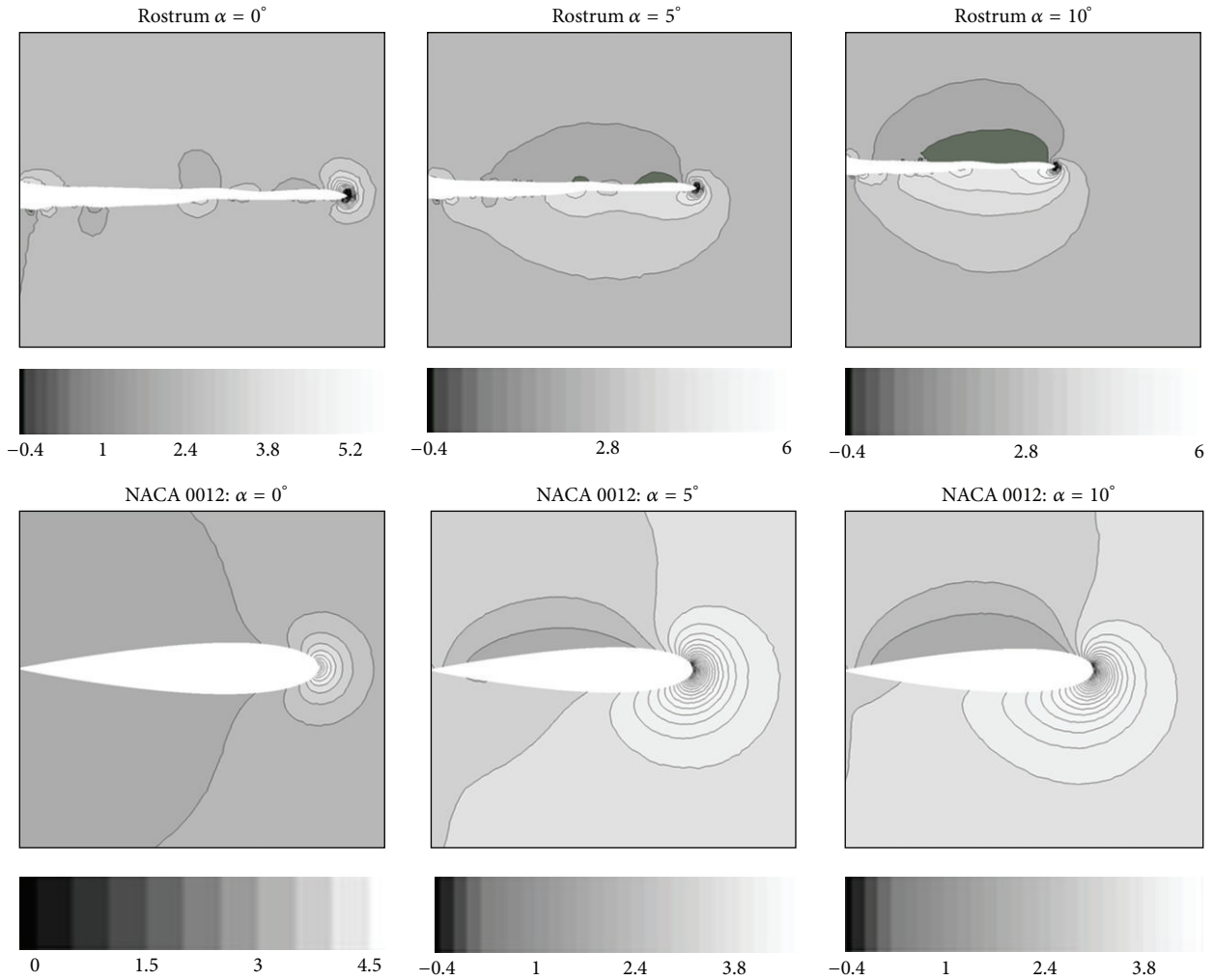


FIGURE 6: Pressure coefficient contour plots corresponding to $\alpha = 0^\circ$, $\alpha = 5^\circ$, and $\alpha = 10^\circ$ corresponding to the paddlefish rostrum and the NACA 0012 foil.

TABLE 2: Mesh independence study.

Case	Mesh resolution (no. of elements/ $\langle y^+ \rangle$)	C_l	C_d
Rostrum ($\alpha = 5^\circ$)	1,168,498/30	0.919	0.214
Rostrum ($\alpha = 5^\circ$)	1,285,972/20	0.564	0.176
Rostrum ($\alpha = 5^\circ$)	1,877,423/18	0.564	0.176

5. Results

As a preliminary step, a grid independence study was conducted for the paddlefish rostrum at $\alpha = 5^\circ$. As shown in Table 2, an initial grid resolution of approximately $1.17E6$ elements was initially assigned. This resulted in a viscous wall unit (y^+) of 30 and lift and drag coefficients of 0.919 and 0.214, respectively. Increasing the number of elements to approximately $1.29E6$ resulted in a viscous wall unit of 20 and

lift and drag coefficients of 0.6361 and 0.1683, respectively. Further increasing the resolution to $1.88E6$ elements, while further decreasing the viscous wall unit to 18, confirmed the grid independent results for the lift and drag coefficients. Consequently, a grid resolution of approximately $1.88E6$ elements was used throughout the remainder of this study.

Figure 6 shows contour plots of pressure coefficient, for both the rostrum and the NACA 0012 hydro foil, along the $y = 0$ plane, for each of the three angles of attack. As shown, the pressure coefficient shows the effect of a stagnation condition located at the tips of both bodies and is represented by a rapid pressure increase at this location. A dramatic change in pressure coefficient is observed $\alpha = 5^\circ$ and $\alpha = 10^\circ$, as the pressure along the upper side of the rostrum/foil is decreased while the pressure along the lower side is increased. The magnitude of these pressure differences (for both cases) is observed to increase (over these specified coefficients angles) and serves to account for the increased lift and drag that are reported in what follows.

The lift and drag forces represent a combined effect due to pressure (P) and shear (viscous) stresses (τ_w). In terms of drag force, these effects may be computed as follows:

$$F_{D \text{ (Total)}} = F_{D \text{ (pressure)}} + F_{D \text{ (viscous)}},$$

$$F_{D \text{ (Pressure)}} = \oint P \hat{n} \cdot \hat{e}_d dS, \quad (2)$$

$$F_{D \text{ (viscous)}} = \oint \tau_w \hat{t} \cdot \hat{e}_d dS,$$

where \hat{e}_d is a unit vector parallel to the flow direction, \hat{n} and \hat{t} are unit vectors perpendicular and parallel to the surface of the rostrum, respectively, and S is the total rostrum surface area. Similarly, for the lift force,

$$F_{L \text{ (Total)}} = F_{L \text{ (pressure)}} + F_{L \text{ (viscous)}},$$

$$F_{L \text{ (Pressure)}} = \oint P \hat{n} \cdot \hat{e}_l dS, \quad (3)$$

$$F_{L \text{ (viscous)}} = \oint \tau_w \hat{t} \cdot \hat{e}_l dS,$$

where \hat{e}_l is a unit vector perpendicular to the flow direction. The drag coefficient (C_d) and lift coefficient (C_l) can thus be computed from the following:

$$C_d = \frac{F_{D \text{ (Total)}}}{1/2 \rho v^2 A}, \quad (4)$$

$$C_l = \frac{F_{L \text{ (Total)}}}{1/2 \rho v^2 A},$$

where ρ is the static pressure, v is the free-stream velocity, and A is the planform area (i.e., the projection of the rostrum (or foil) onto the z -plane, $A = 0.019 \text{ m}^2$).

Table 3 summarizes the results for the paddlefish rostrum, including the lift and drag force coefficients at three angles of attack (0° , 5° , and 10°). For comparison purposes, the rostrum results are accompanied by results pertaining to the NACA 0012 and N22 hydrofoils. While the NACA 0012 foil results were obtained by conducting additional 3D numerical simulations, the N22 results were obtained from the available literature [25].

The NACA 0012 foil (as shown in Figure 7) is symmetric about its chord with 12% thickness and 0% camber at 30% chord length. The hydrofoil was created from a series of x/z point data [26] and extruded in the y -direction an amount equivalent to the area ($A = 0.019 \text{ m}^2$) projected by the rostrum. The remainder of the simulation parameters for the hydrofoil were identical to those conducted for the rostrum (see Section 4), including the grid resolution.

The N22 foil (also shown in Figure 7) is asymmetric about its chord with a maximum thickness of 12.4% and a 6.2% camber at 30% chord length. Since a separate set of simulations was not conducted for this foil, the results presented in Table 3 correspond to section lift and drag coefficients taken from the literature, wherein the chord length (l) is used instead of the planform area (A) in (4). This

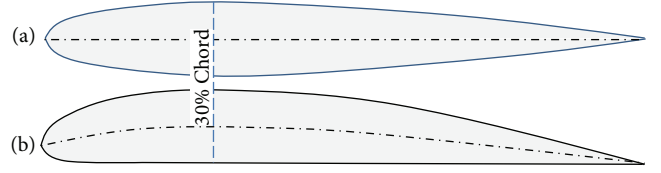


FIGURE 7: The NACA 0012 (symmetric) foil (a) the N22 cambered foil (b).

TABLE 3: Lift and drag coefficients for three angles of attack ($Rn = 1.3E5$).

Case	(α)	C_l	C_d
Rostrum	0°	0.024	0.119
Rostrum	5°	0.564	0.176
Rostrum	10°	1.005	0.346
NACA 0012	0°	0.0	0.017
NACA 0012	5°	0.614	0.018
NACA 0012	10°	0.974	0.047
N22	0°	0.64	0.017
N22	5°	1.157	0.022
N22	10°	1.491	0.036

effect corresponds to a two-dimensional foil with an infinite span (length along the z -axis). For comparison purposes, this simplification results in lift and drag coefficients that can be somewhat higher than actual values.

From Table 3, in contrast to the symmetric airfoil, the rostrum does experience a small amount of lift ($C_l = 0.024$) at $\alpha = 0^\circ$. This however is only minimal when compared to the lift coefficient of 0.64 associated with the cambered foil at $\alpha = 0^\circ$. At $\alpha = 5^\circ$, the rostrum lift coefficient increases dramatically to $C_l = 0.564$, which is only 8.5% less than the lift experienced by the NACA 0012 foil. At $\alpha = 5^\circ$, the N22 foil experiences a lift coefficient of approximately 1.2. At $\alpha = 10^\circ$, the rostrum continues to demonstrate reasonable lift capability, actually surpassing the NACA0012, with respective lift coefficients of 1.0 and 0.97, respectively. The cambered foil, meanwhile, has increased its lift to approximately 1.5 at $\alpha = 10^\circ$.

In terms of the drag coefficient, the rostrum is seen to produce significantly more total drag than either of the two foils. At all angles of attack, the rostrum drag coefficient is 6–8 times that of either of the other two foils.

Table 4 shows the rostrum lift and drag components pertaining to the contributions from pressure and viscous forces, as well as the integrated total lift and drag force over the entire rostrum surface (see (2)-(3)). As indicated, by far the most significant contributions arise from pressure forces, with only minimal viscous force contribution.

The pressure coefficient (C_p) is expressed as follows:

$$C_p = \frac{(P - P_{\text{ref}})}{1/2 \rho v^2}, \quad (5)$$

where P is the static pressure and P_{ref} is the reference pressure ($P_{\text{ref}} = 0$ gauge). Figure 8 shows a plot of the pressure

TABLE 4: Rostrum lift and drag components pertaining to the contributions from pressure and viscous forces, as well as the integrated total lift and drag force over the entire rostrum surface (see (2)-(3)).

(α)	$C_{l(\text{press.})}$	$C_{l(\text{visc.})}$	$F_{L(\text{Tot.})}$ (N)	$C_{d(\text{press.})}$	$C_{d(\text{visc.})}$	$F_{D(\text{Tot.})}$ (N)
0°	0.0244	0.0001	0.0552	0.0663	0.0526	0.2703
5°	0.5677	-0.0041	1.5081	0.1233	0.0523	0.3991
10°	1.0137	-0.0083	2.9668	0.2950	0.0514	0.7870

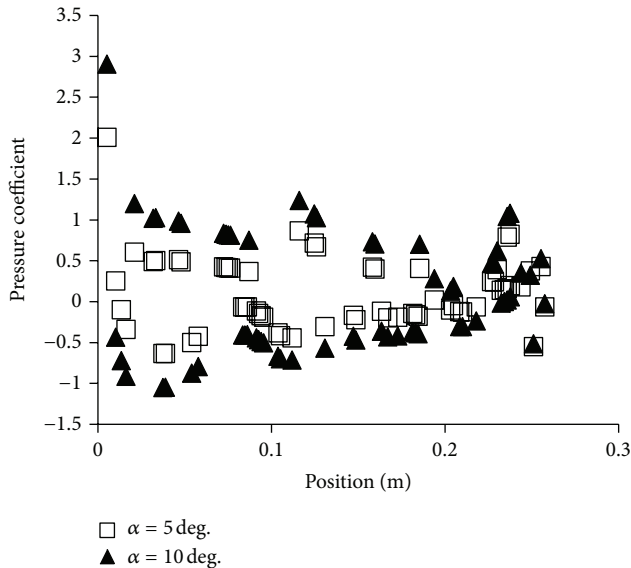


FIGURE 8: Pressure coefficients integrated over the rostrum surface, corresponding to $\alpha = 5^\circ$ and $\alpha = 10^\circ$.

coefficient (C_p) for $\alpha = 5^\circ$ and $\alpha = 10^\circ$, integrated over the surface of the rostrum. In Figure 8, the lower data (with negative pressure coefficients) correspond to the upper surface of the rostrum, while the upper data correspond to the lower surface of the rostrum. Clearly, these differences in pressure are responsible for the significant amount of lift that the rostrum generates.

6. Conclusions

The results presented herein suggest that the paddlefish rostrum does indeed produce a significant amount of lift at certain elevated angles of attack. In fact, the results indicate that the amount of lift is comparable to that produced by a symmetric airfoil (NACA 0012). When compared to a cambered foil (N22), however, the rostrum performs only marginally. It was observed that, in contrast to viscous forces, the majority of this lift occurred as a result of pressure forces. At the neutral position ($\alpha = 0^\circ$), the lift produced by the rostrum was only slightly superior to that by a symmetric foil. In terms of hydrodynamic efficiency, this favorable amount of lift (at all angles of attack) was somewhat offset by the substantial amount of drag (primarily pressure drag) that occurs simultaneously.

Owing to the various assumptions made in this study, primarily including the nonslip surface boundary condition,

and the fact that only the rostrum was modeled (i.e., the paddlefish head and mouth geometries were neglected), the results presented here may be regarded only as a first approximation. Future studies may wish to evaluate the effect of assigning slip velocities as the rostrum surface, a likely possibility, since most fish develop a mucous layer covering their entire bodies in order to reduce the viscous drag [27]. A more representative model, which includes more of the fish's forward anatomy, would also be beneficial.

Conflict of Interests

The authors declare that there is no conflict of interests regarding the publication of this paper.

Acknowledgments

This research was performed as part of the US Army Engineer Research and Development Center Directed Research Programs. In particular, the authors gratefully acknowledge the funding support from the research programs: "Biostructural Analysis and Modeling: the Paddlefish Rostrum as a Structure for Bioinspiration." The authors thank the Chief of Engineers of the US Army Corps of Engineers for permission to publish this paper.

References

- [1] J. D. Pettigrew and L. Wilkens, "Paddlefish and platypus: parallel evolution of passive electroreception in a rostral bill organ," *Sensory Processing in Aquatic Environments*, pp. 420–433, 2003.
- [2] C. P. Paukert and G. D. Scholten, *Paddlefish Management, Propagation, and Conservation in the 21st Century*, American Fisheries Society Symposium 66, Bethesda, Md, USA, 2009.
- [3] V. M. Pitman, *Synopsis of Paddlefish Biology and Their Utilization and Management in Texas*, Special Report, Texas Parks and Wildlife Dept., Fisheries and Wildlife Division, Inland Fisheries Branch, Austin, Tex, USA, 1991.
- [4] P. D. Southall and W. A. Hubert, "Habitat use by adult paddlefish in the upper Mississippi River," *Transactions of the American Fisheries Society*, vol. 113, no. 2, pp. 125–131, 1984.
- [5] S. T. Ross, *The Inland Fishes of Mississippi*, University Press of Mississippi, Jackson, 2001.
- [6] L. A. Wilkens, B. Wettring, E. Wagner, W. Wojtenek, and D. Russell, "Prey detection in selective plankton feeding by the paddlefish: is the electric sense sufficient?" *Journal of Experimental Biology*, vol. 204, no. 8, pp. 1381–1389, 2001.
- [7] J. Mørup Jørgensen, Å. Flock, and J. Wersäll, "The lorenzian ampullae of *Polyodon spathula*," *Zeitschrift für Zellforschung und Mikroskopische Anatomie*, vol. 130, no. 3, pp. 362–377, 1972.

- [8] D. F. Russett, L. A. Wilkens, and F. Moss, "Use of behavioural stochastic resonance by paddle fish for feeding," *Nature*, vol. 402, no. 6759, pp. 291–294, 1999.
- [9] L. A. Wilkens, D. F. Russell, X. Pei, and C. Gurgens, "The paddlefish rostrum functions as an electrosensory antenna in plankton feeding," *Proceedings of the Royal Society B*, vol. 264, no. 1389, pp. 1723–1729, 1997.
- [10] P. W. Smith, *The Fishes of Illinois*, University of Illinois Press, Urbana, Ill, USA, 1979.
- [11] Autodesk, 3ds Max, 2010, <http://usa.autodesk.com>.
- [12] Fluent, Gambit User's Guide, 2004, <http://www.fluent.com/software>.
- [13] H. K. Versteeg and W. Malalasekera, *An Introduction To Computational Fluid Dynamics*, Longman Group Ltd, Essex England, 1995.
- [14] J. B. Allen and D. L. Smith, "Characterizing the impact of geometric simplification on large woody debris using CFD," *International Journal of Hydraulic Engineering*, vol. 1, no. 2, pp. 1–14, 2012.
- [15] D. A. Lyn and W. Rodi, "Flapping shear layer formed by flow separation from the forward corner of a square cylinder," *Journal of Fluid Mechanics*, vol. 267, pp. 353–376, 1994.
- [16] D. A. Lyn, S. Einav, W. Rodi, and J.-H. Park, "Laser-Doppler velocimetry study of ensemble-averaged characteristics of the turbulent near wake of a square cylinder," *Journal of Fluid Mechanics*, vol. 304, pp. 285–319, 1995.
- [17] B. E. Launder and D. B. Spalding, "The numerical computation of turbulent flows," *Computer Methods in Applied Mechanics and Engineering*, vol. 3, no. 2, pp. 269–289, 1974.
- [18] V. Yakhot and L. M. Smith, "The renormalization group, the ϵ -expansion and derivation of turbulence models," *Journal of Scientific Computing*, vol. 7, no. 1, pp. 35–61, 1992.
- [19] F. R. Menter, "Two-equation eddy-viscosity turbulence models for engineering applications," *AIAA journal*, vol. 32, no. 8, pp. 1598–1605, 1994.
- [20] R. Verstappen and A. Veldman, *Fourth-Order DNS of Flow Past a square Cylinder: First Results*, Department of Mathematics, University of Groningen, The Netherlands, <http://ercoftac.mech.surrey.ac.uk/LESig/les2>.
- [21] K. Nozawa and T. Tamura, *LES of Flow Past a square Cylinder Using Embedded Meshes*, Izumi Research Institute and Tokio Institute of Technology, Japan.
- [22] G. T. O. LeBreton and R. S. McKinley, *Sturgeons and Paddlefish of North America*, Kluwer Academic Publishing, Dordrecht, The Netherlands, 2004.
- [23] Fluent 6.3 Users Guide, Lebanon NH, 2006.
- [24] R. I. Issa, "Solution of the implicitly discretised fluid flow equations by operator-splitting," *Journal of Computational Physics*, vol. 62, no. 1, pp. 40–65, 1986.
- [25] T. J. Mueller, "Aerodynamic measurements at low reynolds numbers for fixed wing micro-air vehicles," in *Development and Operation of UAVs For Military and Civil Applications*, VKI, Belgium, 1999.
- [26] 2013, <http://airfoiltools.com>.
- [27] D. M. Bushnell and K. J. Moore, "Drag reduction in nature," *Annual Review of Fluid Mechanics*, vol. 23, no. 1, pp. 65–79, 1991.



Hindawi

Submit your manuscripts at
<http://www.hindawi.com>

